

₁ Physics-Infused Reduced-Order Modeling for Analysis of
₂ Ablating Hypersonic Thermal Protection Systems

₃

₄ November 15, 2025

₅

Abstract

₆ This work presents a *physics-infused reduced-order modeling* (PIROM) framework
₇ towards the design, analysis, and optimization of non-decomposing ablating hyper-
₈ sonic thermal protection systems (TPS). It is demonstrated via the modeling of tran-
₉ sient thermo-ablative behavior of non-decomposing multi-layered hypersonic TPS. The
₁₀ PIROM architecture integrates a reduced-physics backbone, based on the lumped-
₁₁ capacitance model (LCM), with data-driven correction dynamics formulated via a
₁₂ coarse-graining approach rooted in the Mori-Zwanzig formalism. The LCM is coupled
₁₃ to a surface velocity model (SVM) to capture the recession of the ablating TPS as a
₁₄ function of the surface temperature. While the LCM and SVM capture the dominant
₁₅ physics of the ablating TPS response, the correction terms compensate for residual
₁₆ dynamics arising from higher-order non-linear interactions and heterogeneities across
₁₇ material layers. The PIROM consistently achieves errors below 1% for a wide range of
₁₈ extrapolative settings of design parameters involving time-and-space varying boundary
₁₉ conditions and SVM models, and improves by $x\%$ over the LCM alone. Moreover, the
₂₀ PIROM delivers online evaluations that are two orders of magnitude faster than the
₂₁ full-order model (FOM). These results demonstrate that PIRO effectively reconciles
₂₂ the trade-offs between accuracy, generalizability, and efficiency, providing a promising

23 framework for optimizing multi-physical dynamical systems, such as TPS under diverse
24 operating conditions.

25 1 Introduction

26 At hypersonic speeds, aerospace vehicles experience extreme aero-thermo-dynamic environ-
27 ments that require specialized thermal protection systems (TPS) to shield internal sub-
28 structures, electronics, and possibly crew members from the intense aerodynamic heating.
29 The TPS is often composed of ablating materials – a high-temperature capable fibrous
30 material injected with a resin that fills the pore network and strengthens the compos-
31 ite [Amar2016](#). The TPS design promotes the exchange of mass through thermal and
32 chemical reactions (i.e., pyrolysis), effectively mitigating heat transfer to the sub-structures.

33 As a result, accurate prediction for the ablating TPS response under extreme hyper-
34 sonic heating becomes fundamental to ensuring survivability, performance, and safety of
35 hypersonic vehicles. Not only is it necessary to assess the performance of the thermal man-
36 agement systems, but also the shape changes of the vehicle’s outer surface induced by the
37 ablating material, and its impact on the aerodynamics, structural integrity, and controlla-
38 bility. Nonetheless, high-fidelity simulations of ablating TPS remains a formidable challenge
39 both theoretically and computationally.

40 Unfortunately, high-fidelity simulations of ablating TPS remains a formidable challenge
41 both theoretically and computationally.

42 On the theoretical side, the thermo-chemical reactions, coupled with the irregular pore
43 network structure, translate into simplifying assumptions to reduce non-linearities, and make
44 the resulting equations more amenable for engineering application and design analysis [x](#).
45 For instance, one of the most notable codes is the one-dimensional [CMA](#) code that was
46 developed by Aerotherm Corporation in the 1960s [Howard2015](#). Despite its practical use
47 in...

48 Another example is the CHarring Ablator Response (CHAR) ablation code, which ignores
49 elemental decompositions of the pyrolyzing gases, assumes the gases to be a mixture of perfect
50 gases in thermal equilibrium, and assumes no reaction or condensation with the porous
51 network [1].

52 In sum, the objectives of this work are as follows:

- 53 1. Extend the previous formulation from Ref. [12] to model the transient thermo-ablative
54 response of multi-layered hypersonic TPS through a systematic coarse-graining proce-
55 dure based on the Mori-Zwanzig formalism.
- 56 2. Benchmark the accuracy, generalizability, and computational efficiency of the PIROM
57 against the RPM and the high-fidelity FEM solutions of ablating TPS, thus demon-
58 strating the PIROM's potential to solve the ITM in complex multi-physical non-linear
59 dynamical systems.

60 **2 Modeling of Ablating Thermal Protection Systems**

61 This section presents the problem of modeling a non-decomposing ablating TPS subjected to
62 extreme hypersonic heating. Two different but mathematically connected solution strategies
63 are provided: (1) a high-fidelity full-order model (FOM) based on a finite element method
64 (FEM), and (2) a low-fidelity reduced-physics model (RPM) based on a lumped capacitance
65 model (LCM) and a one-dimensional surface velocity model (SVM). The FOM is compu-
66 tationally expensive but provides the highest fidelity, while the RPM is computationally
67 efficient but has low predictive fidelity; both models are amenable to high-dimensional de-
68 sign variables. The RPM is used in the subsequent sections for deriving the PIROM.

69 **2.1 Governing Equations**

70 The multi-physics for a non-decomposing ablating TPS involves the *energy equation* which
71 models the transient heat conduction inside the TPS, and the *pseudo-elasticity equation*,

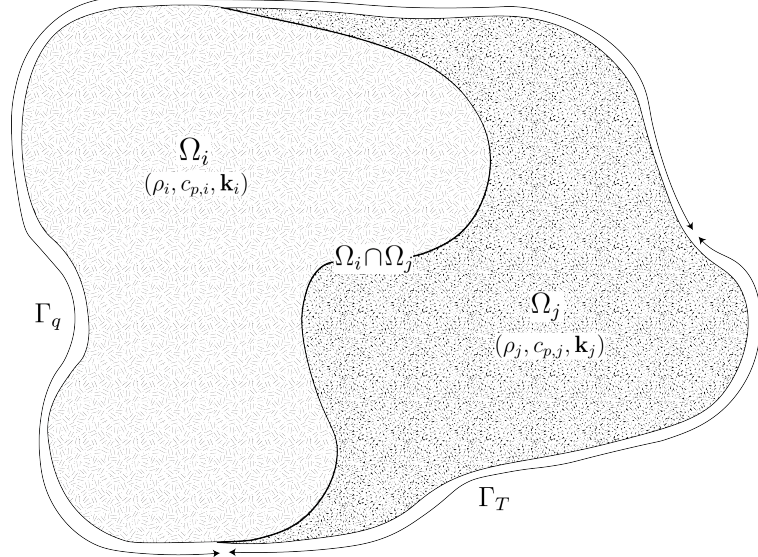


Figure 1: General domain Ω with prescribed Neumann and Dirichlet boundary conditions on Γ_q and Γ_T . Mesh displacement $w(x, t)$ occurs on the Γ_q boundary.

72 which models the mesh motion due to surface recession. The governing PDEs for the ablating
 73 TPS are summarized in this section.

74 2.1.1 Energy Equation

75 Consider a generic domain $\Omega \subset \mathbb{R}^d$, $d = 2$ or 3 , illustrated in Fig. 1. Let $\partial\Omega = \Gamma_q \cup \Gamma_T$ and
 76 $\Gamma_q \cap \Gamma_T = \emptyset$, where a Neumann $q_b(x, t)$ boundary condition is prescribed on the Γ_q boundary,
 77 and represents the surface exposed to the hypersonic boundary layer. The Dirichlet $T_b(x, t)$
 78 boundary condition is prescribed on the boundary Γ_T . The TPS is divided into N non-
 79 overlapping components $\{\Omega_i\}_{i=1}^N$, as illustrated in Fig. 1 for $N = 2$. The i -th component Ω_i
 80 is associated with material properties $(\rho_i, c_{p,i}, \mathbf{k}_i)$, that are assumed to be continuous within
 81 one component, and can be discontinuous across two neighboring components.

82 The transient heat conduction is described by the energy equation,

$$\rho c_p \left(\frac{\partial T}{\partial t} + \tilde{\mathbf{v}}(x, t) \cdot \nabla T \right) - \nabla \cdot (\mathbf{k} \nabla T) = 0, \quad x \in \Omega \quad (1a)$$

$$-\mathbf{k} \nabla T \cdot \mathbf{n} = q_b(x, t), \quad x \in \Gamma_q \quad (1b)$$

$$T(x, t) = T_b(x, t), \quad x \in \Gamma_T \quad (1c)$$

$$T(x, 0) = T_0(x), \quad x \in \Omega \quad (1d)$$

83 where the density ρ is constant, while the heat capacity c_p and thermal conductivity $\mathbf{k} \in \mathbb{R}^{d \times d}$
 84 may depend on temperature. In the order they appear, the terms in eq. (1a) include, the
 85 unsteady energy storage, heat conduction, temperature advection due to mesh motion, and
 86 source terms due to boundary conditions. The boundary conditions for the energy equation
 87 includes Neumann eq. (1b) and Dirichlet eq. (1c) on Γ_T .

88 An Abirtrary Lagrangian-Eulerian (ALE) description is used to account for mesh motion
 89 due to surface recession, where $\tilde{\mathbf{v}}(x, t)$ is the relative velocity of the material with respect to
 90 the mesh,

$$\tilde{\mathbf{v}}(x, t) = \mathbf{v}_s(x, t) - \mathbf{v}_m(x, t) \quad (2)$$

91 where $\mathbf{v}_s(x, t)$ and $\mathbf{v}_m(x, t)$ are the physical material velocity and mesh velocity, respectively.
 92 In this work, the physical material velocity is assumed to be zero, i.e., $\mathbf{v}_s(x, t) = \mathbf{0}$, and thus
 93 the relative velocity is simply the negative of the mesh velocity, $\tilde{\mathbf{v}}(x, t) = -\mathbf{v}_m(x, t)$.

⁹⁴ **2.1.2 Pseudo-Elasticity Equation**

⁹⁵ The mesh motion is described by the steady-state pseudo-elasticity equation without body
⁹⁶ forces,

$$\nabla \cdot \boldsymbol{\sigma}(\mathbf{w}) = \mathbf{0}, \quad \forall t \in \mathcal{T}, \mathbf{x} \in \Omega \quad (3a)$$

$$\mathbf{w}(\mathbf{x}, t) = \mathbf{w}_q(\mathbf{x}, t), \quad \forall t \in \mathcal{T}, \mathbf{x} \in \Gamma_q \quad (3b)$$

$$\mathbf{w}(\mathbf{x}, t) = \mathbf{0}, \quad \forall t \in \mathcal{T}, \mathbf{x} \notin \Gamma_q \quad (3c)$$

$$\mathbf{w}(\mathbf{x}, 0) = \mathbf{0}, \quad \forall \mathbf{x} \in \Omega \quad (3d)$$

⁹⁷ where the stress tensor $\boldsymbol{\sigma}$ is related to the strain tensor $\boldsymbol{\epsilon}(\mathbf{w})$ through Hooke's law,

$$\boldsymbol{\sigma}(\mathbf{w}) = \mathbb{D} : \boldsymbol{\epsilon}(\mathbf{w})$$

⁹⁸ where \mathbb{D} is the fourth-order positive definite elasticity tensor, and ":" is the double con-
⁹⁹ traction of the full-order tensor \mathbb{D} with the second-order tensor $\boldsymbol{\epsilon}$. The elasticity tensor
¹⁰⁰ ordinarily possess a number of symmetries, effectively reducing the number of components
¹⁰¹ that describe it [2]. The symmetric strain tensor $\boldsymbol{\epsilon}$ measures the deformation of the mesh
¹⁰² due to displacements $\mathbf{w}(x, t)$, and is defined as,

$$\boldsymbol{\epsilon}(\mathbf{w}) = \frac{1}{2} (\nabla \mathbf{w} + \nabla \mathbf{w}^\top)$$

¹⁰³ The "material" properties for the mesh are chosen to tailor the mesh deformation, and need
¹⁰⁴ not represent the actual material being modeled [1].

¹⁰⁵ For the pseudo-elasticity equations, the boundary conditions include prescribed displace-
¹⁰⁶ ments $\mathbf{w}_q(x, t)$ on the heated boundary Γ_q in eq. (3b), and zero displacements on the unheated
¹⁰⁷ boundaries in eq. (3c). The initial condition for the mesh displacements is zero in eq. (3d).
¹⁰⁸ Particularly, the surface velocity due to the ablating material is a function of the surface

¹⁰⁹ temperature $T_q(x, t)$ for $x \in \Gamma_q$ on the heated boundary. For the i -th material component,
¹¹⁰ the mesh velocity on the heated boundary is imposed based on the following relation,

$$\hat{\mathbf{n}} \cdot \mathbf{v}_m(x, t) = f(T_q(x, t)), \quad x \in \Gamma_q \quad (4)$$

¹¹¹ where $\hat{\mathbf{n}}$ is the unit normal vector on the heated boundary Γ_q , and f is a function obtained
¹¹² from tabulated data for the material, commonly referred to as a B' table [1]. The B' table
¹¹³ provides a model for the recession velocity as a function of the surface temperature, and is
¹¹⁴ pre-computed based on high-fidelity simulations of the ablation process for a one-dimensional
¹¹⁵ slab of the material, and is independent of the TPS geometry. Provided the surface velocity,
¹¹⁶ the boundary condition in eq. (5) for the mesh displacements are computed by integrating
¹¹⁷ the surface velocity over time,

$$\mathbf{w}_q(x, t) = \int_0^t \mathbf{v}_m(x, \tau) d\tau \quad (5)$$

¹¹⁸ 2.2 Full-Order Model: Finite-Element Method

¹¹⁹ To obtain the full-order numerical solution, the *energy equation* is spatially discretized using
¹²⁰ variational principles of the Discontinuous Galerkin (DG) method [5]. Note that the choice
¹²¹ of DG approach is mainly for theoretical convenience, and is exclusively performed on the
¹²² energy equation, as it is the surface temperature that drives the ablation process. The
¹²³ equivalence between DG and FEM is noted upon their convergence. For the *pseudo-elasticity*
¹²⁴ *equation* standard FEM is used to compute the mesh displacements based on the surface
¹²⁵ temperature provided by the DG solution of the energy equation [2].

¹²⁶ Consider a conforming mesh partition domain, where each element belongs to one and
¹²⁷ only one component. Denote the collection of all M elements as $\{E_i\}_{i=1}^M$. In an element E_i ,
¹²⁸ its shared boundaries with another element E_j , Neumann BC, and Dirichlet BC are denoted
¹²⁹ as e_{ij} , e_{iq} , and e_{iT} , respectively. Lastly, $|e|$ denotes the length ($n_d = 2$) or area ($n_d = 3$) of a

¹³⁰ component boundary e .

¹³¹ For the i -th element, use a set of P trial functions, such as polynomials, to represent the
¹³² temperature distribution,

$$T_i(x, t) = \sum_{l=1}^P \phi_l^i(x) u_l^i(t) \equiv \boldsymbol{\phi}_i^\top(x) \mathbf{u}_i(t), \quad i = 1, 2, \dots, M \quad (6)$$

¹³³ Without loss of generality, the trial functions are assumed to be orthogonal, so that,

$$\int_{E_i} \phi_l^i(x) \phi_k^i(x) d\Omega = 0, \quad l \neq k$$

¹³⁴ where δ_{lk} is the Kronecker delta function. Furthermore, for simplicity, choose $\phi_1^i = 1$. Thus,
¹³⁵ by orthogonality,

$$\int_{E_i} \phi_1^i(x) d\Omega = |E_i|, \quad \int_{E_i} \phi_k^i(x) d\Omega = 0, \quad k = 2, 3, \dots, P$$

¹³⁶ Under the choice of basis functions, u_1^i is simply the average temperature of element E_i ,
¹³⁷ denoted as \bar{u}_i .

¹³⁸ By standard variational processes, e.g., [5], the element-wise governing equation is de-
¹³⁹ noted as,

$$\mathbf{A}_i \dot{\mathbf{u}}_i = (\mathbf{B}_i + \mathbf{C}_i) \mathbf{u}_i + \sum_{j \in \mathcal{N}_i \cup \{T_b\}} (\mathbf{B}_{ij}^i \mathbf{u}_i + \mathbf{B}_{ij}^j \mathbf{u}_j) + \mathbf{f}_i(t), \quad \text{for } i = 1, 2, \dots, M \quad (7)$$

¹⁴⁰ which is collected as the following ODE for all the elements in the mesh,

$$\mathbf{A}(\mathbf{u}) \dot{\mathbf{u}} = [\mathbf{B}(\mathbf{u}) + \mathbf{C}(\mathbf{u})] \mathbf{u} + \mathbf{f}(t) \quad (8)$$

¹⁴¹ where $\mathbf{u} = [\mathbf{u}_1, \mathbf{u}_2, \dots, \mathbf{u}_M]^\top \in \mathbb{R}^{MP}$ includes all the DG variables, $\mathbf{f} \in \mathbb{R}^{MP}$ is the exter-
¹⁴² nal forcing, and the system matrices \mathbf{A} , \mathbf{B} , and \mathbf{C} are the matrices due to heat capacity,
¹⁴³ heat conduction, and temperature advection due to mesh motion, respectively. A detailed

¹⁴⁴ derivation of eqs. (7) and (8) and their matrices is provided in Appendix A.

¹⁴⁵ 2.3 Reduced-Physics Model

¹⁴⁶ The RPM for predicting the response of the ablating TPS consists of two components: (1)
¹⁴⁷ the *lumped-capacitance model* (LCM), and (2) the *surface velocity model* (SVM). The LCM is
¹⁴⁸ described as a first-order system of ODEs for predicting the average temperatures inside the
¹⁴⁹ components of the TPS, and provides a low-fidelity (under estimate) for the component's
¹⁵⁰ surface temperature. The SVM provides a relation between the surface temperature and
¹⁵¹ the surface recession velocity based on pre-computed B' tables for the material, enabling the
¹⁵² computation of one-dimensional surface displacements. The LCM and SVM are combined to
¹⁵³ define the RPM, providing low-fidelity estimates for the temperatures and surface recession
¹⁵⁴ of the ablating TPS.

¹⁵⁵ 2.3.1 Lumped Capacitance Model

¹⁵⁶ A general form of the LCM is provided in this section; details regarding the derivation for
¹⁵⁷ the four-component TPS in Fig. 2 are provided in Appendix A. The LCM is a classical
¹⁵⁸ physics-based low-order model for predicting the temporal variation of average temperature
¹⁵⁹ in multiple interconnected components [7]. The LCM is derived at the component level from
¹⁶⁰ a point of view of energy conservation, and leads to the following system of ODEs for the
¹⁶¹ average temperatures on the components,

$$\bar{\mathbf{A}}\dot{\bar{\mathbf{u}}} = \bar{\mathbf{B}}\bar{\mathbf{u}} + \bar{\mathbf{f}}(t) \quad (9)$$

¹⁶² Where the states and inputs,

$$\bar{\mathbf{u}} = [\bar{u}_1, \bar{u}_2, \dots, \bar{u}_N]^\top \in \mathbb{R}^N, \quad \bar{\mathbf{f}} = [\bar{f}_1, \bar{f}_2, \dots, \bar{f}_N]^\top \in \mathbb{R}^N \quad (10)$$

¹⁶³ include the average temperatures $\bar{\mathbf{u}}$ and spatially-integrated inputs $\bar{\mathbf{f}}$ for the N components.
¹⁶⁴ For $i, j = 1, 2, \dots, N$ the (i, j) -th elements of the $\bar{\mathbf{A}} \in \mathbb{R}^{N \times N}$, $\bar{\mathbf{B}} \in \mathbb{R}^{N \times N}$, and $\bar{\mathbf{f}} \in \mathbb{R}^N$
¹⁶⁵ matrices are given by,

$$\bar{A}_i = \begin{cases} \int_{\Omega_i} \rho c_p d\Omega_i, & i = j \\ 0, & i \neq j \end{cases}, \quad \bar{B}_{ij} = \begin{cases} \sum_{j \in \mathcal{N}_i \cup \{T_b\}} \bar{B}_{ij}^i, & i = j \\ \bar{B}_{ij}^{(j)}, & i \neq j \end{cases}, \quad (11a)$$

$$\mathbf{f}_i = \begin{cases} |e_{iq}| \bar{q}_i + \frac{|e_{iT}|}{R_i} \bar{T}_i, & i = j \\ 0, & i \neq j \end{cases} \quad (11b)$$

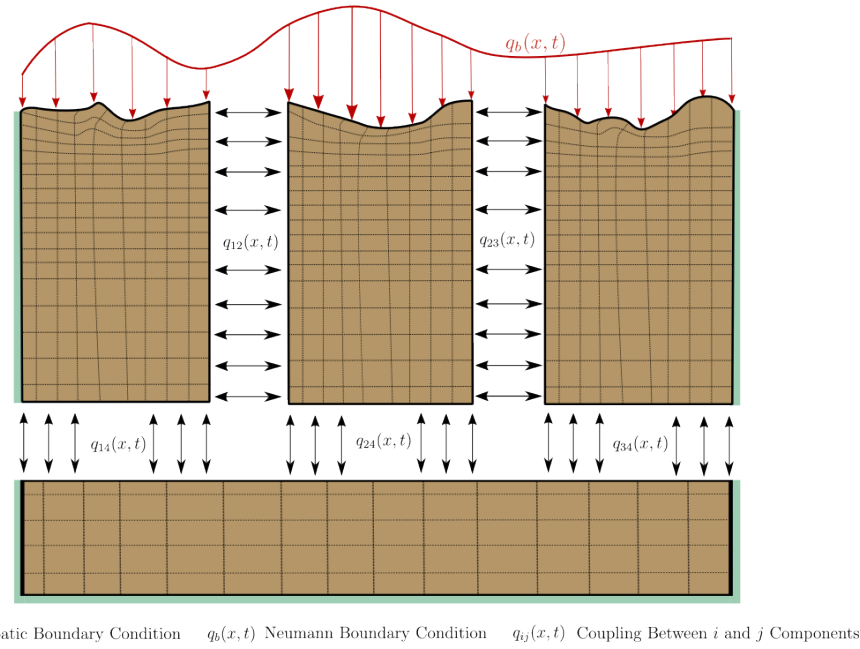
¹⁶⁶ where,

$$\bar{q}_i = \frac{1}{|e_{iq}|} \int_{e_{iq}} q_b de_{iq}, \quad \bar{T}_i = \frac{1}{|e_{iT}|} \int_{e_{iT}} T_b de_{iT}, \quad \bar{B}_{ij}^i = -\frac{|e_{ij}|}{R_{ij}}, \quad \bar{B}_{ij}^j = \frac{|e_{ij}|}{R_{ij}} \quad (12)$$

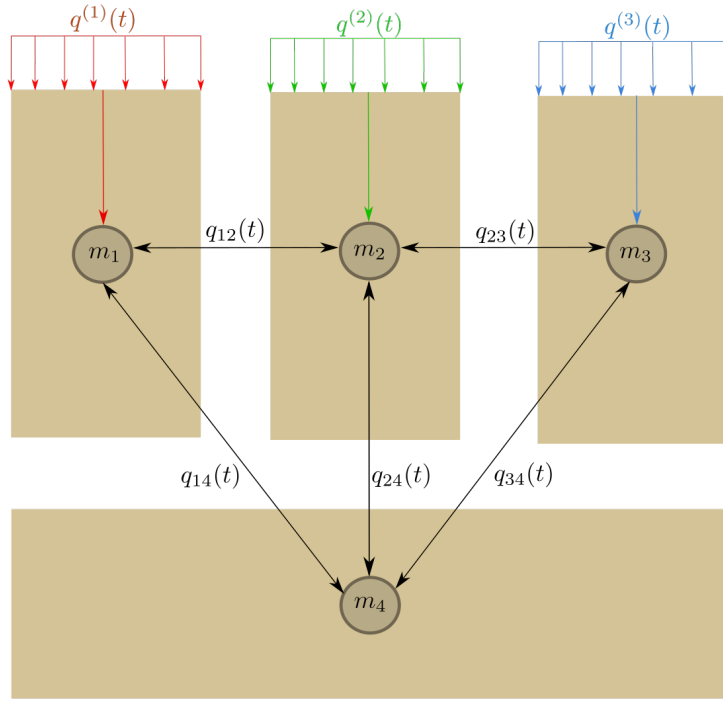
¹⁶⁷ where R_{ij} is the equivalent thermal resistance between two neighboring components Ω_i and
¹⁶⁸ Ω_j , and R_i is the thermal resistance between component Ω_i and the Dirichlet boundary.
¹⁶⁹ The thermal resistances are computed based on the geometry and material properties of the
¹⁷⁰ components; details regarding their computation are provided in Appendix A.

¹⁷¹ 2.3.2 Surface Velocity Model

¹⁷² The displacement is assumed to be *one-dimensional* on the heated boundary Γ_q , i.e., the
¹⁷³ surface recedes only in the direction of the applied load. For example, in Fig. 2, the surface
¹⁷⁴ displacement on the heated boundary occurs only in the negative y -direction for the three
¹⁷⁵ components exposed to the hypersonic boundary layer; the fourth component is the substrate
¹⁷⁶ and does not ablate. Displacements along the x direction is small relative to displacements
¹⁷⁷ in the y direction, and are thus neglected.



(a) TPS Decomposition



(b) Lumped Mass Representation

Figure 2: Partition of the TPS into three ablating and one non-ablating components with the corresponding lumped-mass representation.

¹⁷⁸ For the i -th component, the SVM considered in this work takes the form,

$$\dot{\mathbf{w}} = \Xi \bar{\mathbf{u}} - \tilde{\mathbf{f}} \quad (13)$$

¹⁷⁹ where $\Xi = \text{diag}(\alpha_1, \dots, \alpha_{\tilde{N}})$ and $\tilde{\mathbf{f}} = (\alpha_1 \bar{u}_{0,1}, \dots, \alpha_{\tilde{N}} \bar{u}_{0,\tilde{N}})^\top$. The constants α_i are small
¹⁸⁰ material-dependent constants, determined from the B' table, and $\bar{u}_{0,i}$ is the constant initial
¹⁸¹ temperature of the ablative component. The SVM provides a relation between the surface's
¹⁸² temperature and recession velocity, based on pre-computed B' tables for the material.

¹⁸³ **2.3.3 Coupled Reduced-Physics Model**

¹⁸⁴ The LCM and SVM are combined to define the RPM for predicting the thermo-ablative
¹⁸⁵ response of the TPS under hypersonic boundary layers. Specifically, the RPM is defined as
¹⁸⁶ the LCM as in eq. (9), where the *geometry- and temperature-dependent matrices* $\bar{\mathbf{A}}$, $\bar{\mathbf{B}}$, and
¹⁸⁷ $\bar{\mathbf{f}}$ are updated at each time step based on the current temperature $\bar{\mathbf{u}}$ and displacements \mathbf{w}
¹⁸⁸ provided by the SVM. The RPM is formally stated as,

$$\tilde{\mathbf{A}}(\mathbf{s})\dot{\mathbf{s}} = \tilde{\mathbf{B}}(\mathbf{s})\mathbf{s} + \tilde{\mathbf{F}}(t) \quad (14a)$$

$$\tilde{\mathbf{z}} = \mathbf{I}\mathbf{s} \quad (14b)$$

¹⁸⁹ where the state $\mathbf{s} = [\bar{\mathbf{u}}, \mathbf{w}]^\top \in \mathbb{R}^{2N}$ includes the *average temperature* and *one-dimensional*
¹⁹⁰ *surface displacements*; these are used in the observable outputs $\mathbf{z} = [\bar{\mathbf{u}}, \mathbf{w}]^\top \in \mathbb{R}^{N+\tilde{N}}$, where
¹⁹¹ \tilde{N} is the number of ablating components and $\tilde{N} \leq N$. The matrices are given as,

$$\tilde{\mathbf{A}}(\mathbf{s}) = \begin{bmatrix} \bar{\mathbf{A}}(\mathbf{s}) & \mathbf{0} \\ \mathbf{0} & \mathbf{I} \end{bmatrix}, \quad \tilde{\mathbf{B}}(\mathbf{s}) = \begin{bmatrix} \bar{\mathbf{B}}(\mathbf{s}) & \mathbf{0} \\ \Xi & \mathbf{0} \end{bmatrix}, \quad \tilde{\mathbf{F}}(t) = \begin{bmatrix} \bar{\mathbf{f}}(t) \\ -\tilde{\mathbf{f}} \end{bmatrix} \quad (15)$$

¹⁹² In the matrices $\tilde{\mathbf{A}}$ and $\tilde{\mathbf{B}}$, the surface displacements \mathbf{w} are used to define the dimensions for
¹⁹³ the Ω_i component used in eqs. (11b) and (12), thus effectively coupling the LCM and SVM.

¹⁹⁴ 2.4 Summary of Modeling Approaches

¹⁹⁵ The FOM (i.e., FEM) and RPM (i.e., LCM with SVM) are two different but mathemati-
¹⁹⁶ cally connected solution strategies. Particularly, the LCM in eq. (9) not only resembles the
¹⁹⁷ functional form of the DG model in eq. (8), but can be viewed as a special case of the latter,
¹⁹⁸ where the mesh partition is extremely coarse, and the trial and test functions are piece-wise
¹⁹⁹ constants. This removes all spatial variations within each component, and neglects advection
²⁰⁰ effects due to mesh motion.

²⁰¹ For example, consider the case where each component Ω_i is treated as one single element,
²⁰² and each element employs one constant basis function $\phi_i = 1$. The element-wise DG model
²⁰³ in eq. (7) simplifies into a scalar ODE,

$$\mathbf{A}^{(i)} = \bar{A}_i, \quad \mathbf{C}^{(i)} = 0, \quad \mathbf{B}_{ij}^{(i)} = -\sigma|e_{ij}|, \quad \mathbf{B}_{ij}^{(j)} = \sigma|e_{ij}|, \quad \mathbf{f}_i = |e_{iq}|\bar{q}_i + \sigma|e_{iT}|\bar{T}_i \quad (16)$$

²⁰⁴ Clearly, the LCM is a coarse zeroth-order DG model with the inverse of thermal resistance
²⁰⁵ chosen as the element-wise penalty factors. Or conversely, the DG model is a refined version
²⁰⁶ of LCM via *hp*-adaptation.

²⁰⁷ The FOM and RPM represent two extremes in the modeling fidelity and computational
²⁰⁸ cost spectrum. On one hand, the FOM is the most accurate but computationally expensive
²⁰⁹ to evaluate due to the fine mesh discretizations for both the temperature and displacement
²¹⁰ fields, leading to possibly millions of state variables. On the other hand, the RPM considers
²¹¹ only the average temperature of the material from which one-dimensional surface displace-
²¹² ments are computed. This considerably reduces the computational cost, but sacrifices local
²¹³ temperature information that are critical to properly capture higher-order effects due to
²¹⁴ mesh motion and thermal gradients within each component. Thus, neither the FOM nor
²¹⁵ the RPM is an universal approach for real-world analysis, design, and optimization tasks for
²¹⁶ ablating TPS, where thousands of high-fidelity model evaluations may be necessary. This
²¹⁷ issue motivates the development of the PIROM, which can achieve the fidelity of FOM at

218 a computational cost close to the RPM, while maintaining the generalizability to model
219 parameters.

220 **3 Physics-Infused Reduced-Order Modeling**

221 The formulation of PIROM for ablating TPS starts by connecting the FOM, i.e., the DG-
222 FEM, and the RPM, i.e., the LCM, via a coarse-graining procedure. This procedure pin-
223 points the missing dynamics in the LCM when compared to DG-FEM. Subsequently, the
224 Mori-Zwanzig (MZ) formalism is employed to determine the model form for the missing dy-
225 namics in PIROM. Lastly, the data-driven identification of the missing dynamics in PIROM
226 is presented.

227 **3.1 Deriving the Reduced-Physics Model via Coarse-Graining**

228 The subsequent coarse-graining formulation is performed on the DG-FEM in eq. (8) to derive
229 the LCM in eq. (9). This process constraints the trial function space of a full-order DG model
230 to a subset of piece-wise constants, so that the variables \mathbf{u} , matrices \mathbf{A} , \mathbf{B} , and \mathbf{C} , and forcing
231 vector \mathbf{f} are all approximated using a single state associated to the average temperature.
232 Note that the coarse-graining is exclusively performed on the thermal dynamics, as it is
233 the surface temperature that drives the one-dimensional recession via the SVM. Hence, the
234 coarse-graining of the mesh dynamics is not included in the following procedure.

235 **3.1.1 Coarse-Graining of States**

236 Consider a DG model as in eq. (8) for M elements and an LCM as in eq. (9) for N components;
237 clearly $M \gg N$. Let $\mathcal{V}_j = \{i | E_i \in \Omega_j\}$ be the indices of the elements belonging to the j -th
238 component, so $E_i \in \Omega_j$ for all $i \in \mathcal{V}_j$. The number of elements in the j -th component is $|\mathcal{V}_j|$.

²³⁹ The average temperature on Ω_j is,

$$\bar{u}_j = \frac{1}{|\Omega_j|} \sum_{i \in \mathcal{V}_j} \int_{E^{(i)}} \boldsymbol{\phi}^{(i)}(x)^T \mathbf{u}^{(i)} d\Omega = \frac{1}{|\Omega_j|} \sum_{i \in \mathcal{V}_j} |E_i| \boldsymbol{\varphi}_i^{j\top} \mathbf{u}^{(i)}, \quad j = 1, 2, \dots, N \quad (17)$$

²⁴⁰ where $|\Omega_j|$ and $|E_i|$ denote the area ($d = 2$) or volume ($d = 3$) of component j and element ²⁴¹ i , respectively. The orthogonal basis functions are defined as $\boldsymbol{\varphi}_i^{j\top} = [1, 0, \dots, 0]^\top \in \mathbb{R}^P$.

²⁴² Conversely, given the average temperatures of the N components, $\bar{\mathbf{u}}$, the states of an ²⁴³ arbitrary element E_i is written as,

$$\mathbf{u}^{(i)} = \sum_{k=1}^N \boldsymbol{\varphi}_i^k \bar{u}_k + \delta \mathbf{u}^{(i)}, \quad i = 1, 2, \dots, M \quad (18)$$

²⁴⁴ where $\boldsymbol{\varphi}_i^k = 0$ if $i \notin \mathcal{V}_k$, and $\delta \mathbf{u}^{(i)}$ represents the deviation from the average temperature and ²⁴⁵ satisfies the orthogonality condition $\boldsymbol{\varphi}_i^k \delta \mathbf{u}^{(i)} = 0$ for all k .

²⁴⁶ Equations eqs. (17) and (18) are combined and written in matrix form as,

$$\bar{\mathbf{u}} = \boldsymbol{\Phi}^+ \mathbf{u}, \quad \mathbf{u} = \boldsymbol{\Phi} \mathbf{u} + \delta \mathbf{u} \quad (19)$$

²⁴⁷ where $\boldsymbol{\Phi} \in \mathbb{R}^{MP \times N}$ is a matrix of $M \times N$ blocks, with the (i, j) -th block as $\boldsymbol{\varphi}_i^j$, $\boldsymbol{\Phi}^+ \in \mathbb{R}^{N \times MP}$ ²⁴⁸ is the left inverse of $\boldsymbol{\Phi}$, with the (i, j) -th block as $\boldsymbol{\varphi}_i^{j+} = \frac{|E_i|}{|\Omega_j|} \boldsymbol{\varphi}_i^{j\top}$, and $\delta \mathbf{u}$ is the collection of ²⁴⁹ deviations. By their definitions, $\boldsymbol{\Phi}^+ \boldsymbol{\Phi} = \mathbf{I}$ and $\boldsymbol{\Phi}^+ \delta \mathbf{u} = \mathbf{0}$.

²⁵⁰ 3.1.2 Coarse-Graining of Dynamics

²⁵¹ The dependence of the matrices with respect to the displacements \mathbf{w} is dropped to isolate ²⁵² the analysis based on coarsened variables. Consider a function of states in the form of ²⁵³ $\mathbf{M}(\mathbf{u}) \mathbf{g}(\mathbf{u})$, where $\mathbf{g} : \mathbb{R}^{MP} \rightarrow \mathbb{R}^{MP}$ is a vector-valued function, and $\mathbf{M} : \mathbb{R}^{MP} \rightarrow \mathbb{R}^{p \times MP}$ ²⁵⁴ is a matrix-valued function with an arbitrary dimension p . Define the projection matrix

255 $\mathbf{P} = \Phi\Phi^+$ and the projection operator \mathcal{P} as,

$$\begin{aligned}\mathcal{P}[\mathbf{M}(\mathbf{u})\mathbf{g}(\mathbf{u})] &= \mathbf{M}(\mathbf{P}\mathbf{u})\mathbf{g}(\mathbf{P}\mathbf{u}) \\ &= \mathbf{M}(\Phi\bar{\mathbf{u}})\mathbf{g}(\Phi\bar{\mathbf{u}})\end{aligned}\quad (20)$$

256 so that the resulting function depends only on the average temperatures $\bar{\mathbf{u}}$. Correspondingly,
257 the residual operator $\mathcal{Q} = \mathcal{I} - \mathcal{P}$, and $\mathcal{Q}[\mathbf{M}(\mathbf{u})\mathbf{g}(\mathbf{u})] = \mathbf{M}(\mathbf{u})\mathbf{g}(\mathbf{u}) - \mathbf{M}(\Phi\bar{\mathbf{u}})\mathbf{g}(\Phi\bar{\mathbf{u}})$. When
258 the function is not separable, the projection operator is simply defined as $\mathcal{P}[\mathbf{g}(\mathbf{u})] = \mathbf{g}(\mathbf{P}\mathbf{u})$.

259 Subsequently, the operators defined above are applied to coarse-grain the dynamics. First,
260 write the DG-FEM in eq. (8) as,

$$\dot{\mathbf{u}} = \mathbf{A}(\mathbf{u})^{-1}\mathbf{B}(\mathbf{u})\mathbf{u} + \mathbf{A}(\mathbf{u})^{-1}\mathbf{C}(\mathbf{u})\mathbf{u} + \mathbf{A}(\mathbf{u})^{-1}\mathbf{f}(t) \quad (21)$$

261 and multiply both sides by Φ^+ to obtain,

$$\Phi^+\dot{\mathbf{u}} = \Phi^+(\Phi\dot{\bar{\mathbf{u}}} + \delta\dot{\mathbf{u}}) = \dot{\bar{\mathbf{u}}} = \Phi^+\mathbf{r}(\mathbf{u}, t) \quad (22)$$

262 Apply the projection operator \mathcal{P} and the residual operator \mathcal{Q} to the right-hand side to obtain,

$$\dot{\bar{\mathbf{u}}} = \mathcal{P}[\Phi^+\mathbf{r}(\mathbf{u}, t)] + \mathcal{Q}[\Phi^+\mathbf{r}(\mathbf{u}, t)] \equiv \mathbf{r}^{(1)}(\mathbf{u}, t) + \mathbf{r}^{(2)}(\mathbf{u}, t) \quad (23)$$

263 where $\mathbf{r}^{(1)}(\mathbf{u}, t)$ is resolved dynamics that depends on $\bar{\mathbf{u}}$ only, and $\mathbf{r}^{(2)}(\mathbf{u}, t)$ is the un-resolved
264 or residual dynamics. Detailed derivations and analysis of $\mathbf{r}^{(1)}(\mathbf{u}, t)$ and $\mathbf{r}^{(2)}(\mathbf{u}, t)$ can be
265 found in the Appendix.

266 It follows from Ref. [12] that the resolved dynamics is exactly the LCM, where the
267 advection term reduces to zero, i.e., $\bar{\mathbf{C}}(\bar{\mathbf{u}}) = \mathbf{0}$ as shown in the Appendix. Using the notation

268 from eq. (9), it follows that,

$$\begin{aligned}\mathbf{r}^{(1)}(\mathbf{u}, t) &= \bar{\mathbf{A}}(\bar{\mathbf{u}})^{-1}\bar{\mathbf{B}}(\bar{\mathbf{u}})\bar{\mathbf{u}} + \bar{\mathbf{A}}(\bar{\mathbf{u}})^{-1}\bar{\mathbf{C}}(\bar{\mathbf{u}})\bar{\mathbf{u}} + \bar{\mathbf{A}}(\bar{\mathbf{u}})^{-1}\bar{\mathbf{f}}(\bar{\mathbf{u}}) \\ &= \bar{\mathbf{A}}(\bar{\mathbf{u}})^{-1}\bar{\mathbf{B}}(\bar{\mathbf{u}})\bar{\mathbf{u}} + \bar{\mathbf{A}}(\bar{\mathbf{u}})^{-1}\bar{\mathbf{f}}(t)\end{aligned}\quad (24)$$

269 where the following relations hold,

$$\bar{\mathbf{A}}(\bar{\mathbf{u}}) = \mathbf{W} (\Phi^+ \mathbf{A} (\Phi \bar{\mathbf{u}})^{-1} \Phi)^{-1} \quad \bar{\mathbf{C}}(\bar{\mathbf{u}}) = \mathbf{0} \quad (25a)$$

$$\bar{\mathbf{B}}(\bar{\mathbf{u}}) = \mathbf{W} \Phi^+ \mathbf{B} (\Phi \bar{\mathbf{u}}) \Phi \quad \bar{\mathbf{f}}(t) = \mathbf{W} \Phi^+ \mathbf{f} \quad (25b)$$

270 where $\mathbf{W} \in \mathbb{R}^{N \times N}$ is a diagonal matrix with the i -th element as $[\mathbf{W}]_{ii} = |\mathcal{V}_k|$ if $i \in \mathcal{V}_k$.

271 The examination of the second residual term $\mathbf{r}^{(2)}(\mathbf{u}, t)$ in eq. (23) is shown in the Appendix,
272 and demonstrates that the physical sources of missing dynamics in the LCM include: the
273 approximation of non-uniform temperature within each component as a constant, and the
274 elimination of the advection term due to coarse-graining. In sum, the above results not
275 only show that the LCM is a result of coarse-graining of the full-order DG-FEM, but also
276 reveal the discrepancies between the LCM and the DG-FEM. These discrepancies propagate
277 into the SVM, which as a result of the averaging in the LCM formulation, under-predicts
278 the surface recession rates. In the subsequent section, the discrepancies in the LCM are
279 corrected to formulate the PIROM.

280 3.2 Physics-Infusion Via Mori-Zwanzig Formalism

281 The Mori-Zwanzig (MZ) formalism is an operator-projection technique used to derive ROMs
282 for high-dimensional dynamical systems, especially in statistical mechanics and fluid dynam-
283 ics [9, 10, 11]. It provides an exact reformulation of a high-dimensional Markovian dynamical
284 system, into a low-dimensional observable non-Markovian dynamical system. The proposed
285 ROM is subsequently developed based on the approximation to the non-Markovian term in

the observable dynamics. Particularly, eq. (23) shows that the DG-FEM dynamics can be decomposed into the resolved dynamics $\mathbf{r}^{(1)}(\mathbf{u}, t)$ and the orthogonal dynamics $\mathbf{r}^{(2)}(\mathbf{u}, t)$, in the sense of $\mathcal{P}\mathbf{r}^{(2)} = 0$. In this case, the MZ formalism can be invoked to express the dynamics $\bar{\mathbf{u}}$ in terms of $\bar{\mathbf{u}}$ alone as the projected Generalized Langevin Equation (GLE) [9, 10, 11],

$$\dot{\bar{\mathbf{u}}}(t) = \mathbf{r}^{(1)}(\bar{\mathbf{u}}, t) + \int_0^t \tilde{\kappa}(t, s, \bar{\mathbf{u}}) ds \quad (26)$$

where the first and second terms are referred to as the Markovian and non-Markovian terms, respectively. The non-Markovian term accounts for the effects of past un-resolved states on the current resolved states via a memory kernel $\tilde{\kappa}(t, s, \bar{\mathbf{u}})$, which in practice is computationally expensive to evaluate.

3.2.1 Markovian Reformulation

This section details the formal derivation of the PIROM as a system of ODEs for the thermal dynamics, based on approximations to the memory kernel. Specifically, the kernel $\tilde{\kappa}$ is examined via a leading-order expansion, based on prior work [13]; this can be viewed as an analog of zeroth-order holding in linear system theory with a sufficiently small time step. In this case, the memory kernel is approximated as,

$$\tilde{\kappa}(t, s, \bar{\mathbf{u}}) \approx \mathbf{r}^{(1)}(\bar{\mathbf{u}}, t) \cdot \nabla_{\bar{\mathbf{u}}} \mathbf{r}^{(2)}(\Phi \bar{\mathbf{u}}, t) \quad (27)$$

Note that the terms in $\mathbf{r}^{(1)}$ have a common factor $\bar{\mathbf{A}}^{-1}$; this motivates the following heuristic modification of the model form in eq. (26),

$$\dot{\bar{\mathbf{u}}} = \mathbf{r}^{(1)}(\bar{\mathbf{u}}, t) + \bar{\mathbf{A}}^{-1}(\bar{\mathbf{u}}) \int_0^t \kappa(t, s, \bar{\mathbf{u}}) ds \quad (28a)$$

$$\bar{\mathbf{A}}(\bar{\mathbf{u}}) \dot{\bar{\mathbf{u}}} = \bar{\mathbf{B}}(\bar{\mathbf{u}}) \bar{\mathbf{u}} + \bar{\mathbf{f}}(t) + \int_0^t \kappa(t, s, \bar{\mathbf{u}}) ds \quad (28b)$$

302 where the original kernel $\tilde{\kappa}$ is effectively normalized by $\bar{\mathbf{A}}^{-1}$. Intuitively, such choice of kernel
 303 reduces its dependency on the averaged material properties, and simplifies the subsequent
 304 design of model form.

305 Subsequently, the hidden states are introduced to “Markovianize” the system eq. (26).
 306 In this manner, eq. (28b) is converted into a pure state-space model, with the functional
 307 form of the LCM retained; since LCM is a physics-based model, then it encodes the phys-
 308 ical information and retains explicit parametric dependence of the problem. Consider the
 309 representation of the kernel as a finite sum of simpler functions, e.g., exponentials,

$$\kappa(t, s, \bar{\mathbf{u}}) = \sum_{j=1}^m \mathcal{K}_j(t, s, \bar{\mathbf{u}}) [\mathbf{p}_j + \mathbf{d}_j(\bar{\mathbf{u}})] \phi_j(s, \bar{\mathbf{u}}) \quad (29)$$

310 where,

$$\mathcal{K}_j(t, s, \bar{\mathbf{u}}) = e^{-\int_s^t (\lambda_j + e_j(\bar{\mathbf{u}})) d\tau}, \quad \phi_j(s, \bar{\mathbf{u}}) = \mathbf{q}_j^\top \bar{\mathbf{u}}(s) + \mathbf{g}_j(\bar{\mathbf{u}})^\top \bar{\mathbf{u}}(s) + \mathbf{r}_j^\top \bar{\mathbf{f}}(s) \quad (30)$$

311 with suitable coefficients $\mathbf{p}_j, \mathbf{d}_j, \mathbf{q}_j, \mathbf{g}_j, \mathbf{r}_j \in \mathbb{R}^N$ and decay rates $\lambda_j, e_j(\bar{\mathbf{u}}) > 0$, that need to
 312 be identified from data.

313 Define the hidden states as,

$$\beta_j(t) = \int_0^t \mathcal{K}_j(s, \bar{\mathbf{u}}) \phi_j(s, \bar{\mathbf{u}}) ds \quad (31)$$

314 then through its differentiation with respect to time,

$$\dot{\beta}_j(t) = -[\lambda_j + e_j(\bar{\mathbf{u}})] \beta_j(t) + \mathbf{q}_j^\top \bar{\mathbf{u}}(t) + \mathbf{g}_j(\bar{\mathbf{u}})^\top \bar{\mathbf{u}}(t) + \mathbf{r}_j^\top \bar{\mathbf{f}}(t) \quad (32)$$

315 and the memory term becomes,

$$\int_0^t \kappa(t, s, \bar{\mathbf{u}}) ds = \sum_{j=1}^m [\mathbf{p}_j + \mathbf{d}_j(\bar{\mathbf{u}})] \beta_j(t) \quad (33)$$

³¹⁶ Then, eq. (28b) is recast as the extended Markovian system,

$$\bar{\mathbf{A}}(\bar{\mathbf{u}})\dot{\bar{\mathbf{u}}} = \bar{\mathbf{B}}(\bar{\mathbf{u}})\bar{\mathbf{u}} + [\mathbf{P} + \mathbf{D}(\bar{\mathbf{u}})]\boldsymbol{\beta} + \bar{\mathbf{f}}(t) \quad (34a)$$

$$\dot{\boldsymbol{\beta}} = [\mathbf{Q} + \mathbf{G}(\bar{\mathbf{u}})]\bar{\mathbf{u}} + [\mathbf{E}(\bar{\mathbf{u}}) - \boldsymbol{\Lambda}]\boldsymbol{\beta} + \mathbf{R}\bar{\mathbf{f}}(t) \quad (34b)$$

³¹⁷ where the data-driven operators associated to the hidden dynamics are collected as,

$$\boldsymbol{\Lambda} = \text{diag}(\lambda_1, \lambda_2, \dots, \lambda_m) \in \mathbb{R}^{m \times m}, \quad \mathbf{P} = [\mathbf{p}_1, \mathbf{p}_2, \dots, \mathbf{p}_m] \in \mathbb{R}^{N \times m} \quad (35a)$$

$$\mathbf{D}(\bar{\mathbf{u}}) = [\mathbf{d}_1(\bar{\mathbf{u}}), \mathbf{d}_2(\bar{\mathbf{u}}), \dots, \mathbf{d}_m(\bar{\mathbf{u}})] \in \mathbb{R}^{N \times m}, \quad \mathbf{Q} = [\mathbf{q}_1, \mathbf{q}_2, \dots, \mathbf{q}_m] \in \mathbb{R}^{m \times N} \quad (35b)$$

$$\mathbf{G}(\bar{\mathbf{u}}) = [\mathbf{g}_1(\bar{\mathbf{u}}), \mathbf{g}_2(\bar{\mathbf{u}}), \dots, \mathbf{g}_m(\bar{\mathbf{u}})] \in \mathbb{R}^{m \times N}, \quad \mathbf{R} = [\mathbf{r}_1, \mathbf{r}_2, \dots, \mathbf{r}_m] \in \mathbb{R}^{m \times N} \quad (35c)$$

$$\mathbf{E}(\bar{\mathbf{u}}) = \text{diag}(e_1(\bar{\mathbf{u}}), e_2(\bar{\mathbf{u}}), \dots, e_m(\bar{\mathbf{u}})) \in \mathbb{R}^{m \times m} \quad (35d)$$

³¹⁸ The form of the temperature-dependent matrices $\mathbf{D}(\bar{\mathbf{u}})$, $\mathbf{G}(\bar{\mathbf{u}})$, and $\mathbf{E}(\bar{\mathbf{u}})$ is provided in the
³¹⁹ next section. Note that since the hidden states $\boldsymbol{\beta}$ serve as the memory, their initial conditions
³²⁰ are set to zero, i.e., $\boldsymbol{\beta}(t_0) = \mathbf{0}$, no memory at the beginning. The physics-infused model in
³²¹ eq. (34b) retains the structure of the LCM, while the hidden states account for missing
³²² physics through corrections to the stiffness and advection matrices, as well as the forcing
³²³ term.

³²⁴ 3.2.2 Coupled Physics-Infused Model

³²⁵ The next step involves coupling the physics-infused model in eq. (34b) with the SVM in
³²⁶ eq. (13) to form the PIROM for ablating TPS. To this end, define the observables as the
³²⁷ surface temperature $\mathbf{z}_u \in \mathbb{R}^{\tilde{N}}$ and displacements $\mathbf{z}_w \in \mathbb{R}^{\tilde{N}}$ for $\tilde{N} \leq N$ ablating components
³²⁸ to define the observable vector as $\mathbf{z} = [\mathbf{z}_u, \mathbf{z}_w]^\top \in \mathbb{R}^{n_z}$ with $n_z = 2\tilde{N}$ as the total number of
³²⁹ observables.

³³⁰ Collect the RPM and hidden states into a single state vector $\mathbf{y} = [\bar{\mathbf{u}}, \mathbf{w}, \boldsymbol{\beta}]^\top \in \mathbb{R}^{n_y}$, where
³³¹ $n_y = N + \tilde{N} + m$, and define a data-driven operator $\mathbf{M} \in \mathbb{R}^{n_z \times n_y}$ to define the PIROM's

³³² observable as,

$$\mathbf{z} = \mathbf{M}\mathbf{y} \quad (36)$$

³³³ where,

$$\mathbf{M} = \begin{bmatrix} \mathbf{M}_{\bar{u}} & \mathbf{0} & \mathbf{M}_{\beta} \\ \mathbf{0} & \mathbf{I} & \mathbf{0} \end{bmatrix} \quad (37)$$

³³⁴ includes the matrices $\mathbf{M}_{\bar{u}} \in \mathbb{R}^{\tilde{N} \times N}$ and $\mathbf{M}_{\beta} \in \mathbb{R}^{\tilde{N} \times m}$, which computes the surface tempera-
³³⁵ ture observable from the RPM states and hidden states, respectively. The PIROM is coupled
³³⁶ to the SVM in eq. (13) by leveraging eq. (36) to compute the surface recession velocity. Thus,
³³⁷ the PIROM is formally stated as,

$$\mathcal{A}\dot{\mathbf{y}} = [\mathcal{B} + \mathcal{C}]\mathbf{y} + \mathcal{F}(t) \quad (38a)$$

$$\mathbf{z} = \mathbf{M}\mathbf{y} \quad (38b)$$

³³⁸ where,

$$\mathcal{A} = \begin{bmatrix} \bar{\mathbf{A}} & \mathbf{O} & \mathbf{O} \\ \mathbf{O} & \mathbf{I} & \mathbf{O} \\ \mathbf{O} & \mathbf{O} & \mathbf{I} \end{bmatrix} \in \mathbb{R}^{n_y \times n_y}, \quad \mathcal{B} = \begin{bmatrix} \bar{\mathbf{B}} & \mathbf{O} & \mathbf{P} \\ \Xi\mathbf{M}_u & \mathbf{O} & \Xi\mathbf{M}_{\beta} \\ \mathbf{Q} & \mathbf{O} & -\Lambda \end{bmatrix} \in \mathbb{R}^{n_y \times n_y}, \quad (39a)$$

$$\mathcal{C} = \begin{bmatrix} \mathbf{O} & \mathbf{O} & \mathbf{D}(\bar{\mathbf{u}}) \\ \mathbf{O} & \mathbf{O} & \mathbf{O} \\ \mathbf{G}(\bar{\mathbf{u}}) & \mathbf{O} & \mathbf{E}(\bar{\mathbf{u}}) \end{bmatrix} \in \mathbb{R}^{n_y \times n_y}, \quad \mathcal{F} = \begin{bmatrix} \bar{\mathbf{f}}(t) \\ -\tilde{\mathbf{f}} \\ \mathbf{R}\bar{\mathbf{f}}(t) \end{bmatrix} \in \mathbb{R}^{n_y} \quad (39b)$$

³³⁹ The learnable parameters in the PIROM are collected as,

$$\Theta = \{\mathbf{P}, \mathbf{Q}, \mathbf{R}, \mathbf{D}(\bar{\mathbf{u}}), \mathbf{G}(\bar{\mathbf{u}}), \mathbf{E}(\bar{\mathbf{u}}), \mathbf{M}_u, \mathbf{M}_{\beta}\}, \in \mathbb{R}^{n_{\theta}} \quad (40)$$

³⁴⁰ Particularly, the matrices $\mathbf{P}, \mathbf{A}, \mathbf{Q}, \mathbf{R}$ are constants that need to be identified from data, and
³⁴¹ account for the effects of coarse-graining on the stiffness and forcing matrices. The matrices

342 $\mathbf{D}(\bar{\mathbf{u}})$, $\mathbf{E}(\bar{\mathbf{u}})$, $\mathbf{G}(\bar{\mathbf{u}})$ are state-dependent matrices, and account for the effects of coarse-graining
343 on the advection matrix due to mesh motion. Leveraging the DG-FEM formula for the
344 advection matrix in eq. (52c) in the Appendix, and noting that the ablating velocity in
345 eq. (4) imposes the boundary condition for the mesh motion, the state-dependent matrices
346 for the i -th component are written as,

$$\mathbf{D}(\bar{\mathbf{u}}) \approx \dot{\mathbf{w}}(\bar{\mathbf{u}}) \odot_r \mathbf{D}, \quad \mathbf{G}(\bar{\mathbf{u}}) \approx \mathbf{G} \odot_r \dot{\mathbf{w}}(\bar{\mathbf{u}}), \quad \mathbf{E}(\bar{\mathbf{u}}) \approx \dot{\mathbf{W}}(\bar{\mathbf{u}}) \odot \mathbf{E} \quad (41)$$

347 where $\dot{\mathbf{w}}(\bar{\mathbf{u}})$ is the SVM based on the observable temperature $\bar{\mathbf{u}}$, \odot_r is the row-wise multipli-
348 cation, and $\dot{\mathbf{W}}$ is the concatenation of $\dot{\mathbf{w}}$ for \tilde{m} times, where \tilde{m} corresponds to the number
349 of hidden states per component, i.e., $m = N\tilde{m}$.

350 The PIROM in eq. (38b) incorporates explicit information on the material properties,
351 boundary conditions, and surface recession, and is designed to generalize across parametric
352 variations in these inputs. Moreover, the hidden dynamics in eq. (34b) are interpretable,
353 as these retain the functional form of the DG-FEM in eq. (8). The next step is focused on
354 identifying the unknown data-driven parameters Θ characterizing the hidden dynamics.

355 3.3 Learning the Hidden Dynamics

356 Learning of the PIROM is achieved through a gradient-based neural-ODE-like approach [3].
357 For ease of presentation, consider the compact form of the PIROM in eq. (38b),

$$\mathcal{D}(\dot{\mathbf{y}}, \mathbf{y}, \boldsymbol{\xi}, \mathcal{F}; \Theta) = \mathbf{0} \quad (42)$$

358 where $\boldsymbol{\xi}$ defines the model parameters, i.e., material properties and B' tables, while \mathcal{F}
359 represents the forcing terms, i.e., the boundary conditions.

360 Consider a dataset of N_s high-fidelity *surface temperature* observable trajectories \mathbf{z}_{HF} ,
361 sampled at p time instances $\{t_k\}_{k=0}^{p-1}$, for different parameter settings $\{\boldsymbol{\xi}^{(l)}\}_{l=1}^{N_s}$ and forcing

³⁶² functions $\{\mathcal{F}^{(l)}(t)\}_{l=1}^{N_s}$. The dataset is expressed as,

$$\mathcal{D} = \left\{ \left(t_k, \mathbf{z}_{\text{HF}}^{(l)}(t_k), \boldsymbol{\xi}^{(l)}, \mathcal{F}^{(l)}(t_k) \right) \right\}_{l=1}^{N_s}, \quad k = 0, 1, \dots, p-1 \quad (43)$$

³⁶³ In this work, the dataset contains only surface temperature observables – all high-fidelity
³⁶⁴ information regarding the surface displacements *are assumed to be unavailable during learn-*
³⁶⁵ *ing.*

³⁶⁶ The learning problem is formulated as the following differentially-constrained problem,

$$\min_{\Theta} \quad \mathcal{J}(\Theta; \mathcal{D}) = \sum_{l=1}^{N_s} \int_{t_0}^{t_f} \ell \left(\mathbf{z}_u^{(l)}, \mathbf{z}_{\text{HF}}^{(l)} \right) dt \quad (44a)$$

$$\text{s.t.} \quad \mathbf{0} = \mathcal{D} \left(\dot{\mathbf{y}}^{(l)}, \mathbf{y}^{(l)}, \boldsymbol{\xi}^{(l)}, \mathcal{F}^{(l)}; \Theta \right) \quad (44b)$$

³⁶⁷ for $l = 1, 2, \dots, N_s$, the objective is to minimize the discrepancy between the high-fidelity
³⁶⁸ and PIROM predictions for the l -th trajectory with $\ell \left(\mathbf{z}_u^{(l)}, \mathbf{z}_{\text{HF}}^{(l)} \right) = \left\| \mathbf{z}_u^{(l)} - \mathbf{z}_{\text{HF}}^{(l)} \right\|_2^2$.

³⁶⁹ The gradient-based optimization loop is based on the adjoint variable $\boldsymbol{\lambda}$, governed by the
³⁷⁰ adjoint differential equation,

$$\frac{\partial \ell}{\partial \mathbf{y}} + \boldsymbol{\lambda}^\top \frac{\partial \mathcal{D}}{\partial \mathbf{y}} - \frac{d}{dt} \left(\boldsymbol{\lambda}^\top \frac{\partial \mathcal{D}}{\partial \dot{\mathbf{y}}} \right) = \mathbf{0} \quad (45a)$$

$$\boldsymbol{\lambda}(t_f)^\top \frac{\partial \mathcal{D}}{\partial \dot{\mathbf{y}}(t_f)} = \mathbf{0} \quad (45b)$$

³⁷¹ Once $\boldsymbol{\lambda}$ is solved, the gradient is computed as,

$$\nabla_{\Theta} \mathcal{J} = \frac{1}{N_s} \sum_{l=1}^{N_s} \int_{t_0}^{t_f} \left(\frac{\partial \ell}{\partial \Theta} + (\boldsymbol{\lambda}^{(l)})^\top \frac{\partial \mathcal{D}}{\partial \Theta} \right) dt \quad (46)$$

³⁷² Discussion on TSA?

³⁷³ 4 Application to Thermal Protection Systems

³⁷⁴ In this section, the proposed PIROM approach is applied to the analysis of thermo-ablative
³⁷⁵ multi-layered hypersonic TPS. The performance of the PIROM is evaluated in terms of
³⁷⁶ *accuracy, generalizability, and computational efficiency*, across a range of boundary condition
³⁷⁷ and surface velocity model parametrizations. The results show PIROM to be a promising
³⁷⁸ candidate for the solution of the impossible trinity of modeling.

³⁷⁹ 4.1 Problem Definition

³⁸⁰ Consider the two-dimensional TPS configuration shown in Fig. ³⁸⁰x with constant material
³⁸¹ properties within each layer, dimensions, and BCs listed in Table ³⁸¹x. Such configuration is
³⁸² representative of the TPS used for the initial concept 3.X vehicle in past studies [8], and in-
³⁸³ volves two main layers: an outer ablative layer, and an inner substrate layer. The top ablative
³⁸⁴ layer may be composed of different materials, such as PICA or Avcoat, while the substrate
³⁸⁵ layer is typically made of a high-temperature resistant material, such as carbon-carbon com-
³⁸⁶ posite [6]. The ablative layer, composed of $\tilde{N} = 3$ ablative components, is subjected to
³⁸⁷ strong time-varying and non-uniform heating, while the substrate layer, composed of one
³⁸⁸ non-ablative component, is insulated adiabatically at the outer surface; the total number of
³⁸⁹ components is thus $N = 4$.

³⁹⁰ The sources of non-linearities in the problem originate from the coupling between the
³⁹¹ thermodynamics and the temperature-dependent mesh motion, as well as the heterogeneities
³⁹² across material layers. As shown in Fig. ³⁹²x, perfect thermocouple devices are placed at the
³⁹³ surfaces of the ablative layers for the collection of the high-fidelity temperature signals that
³⁹⁴ are used in the following sections for training and testing the PIROM.

395 **4.2 Parametrization of Boundary Conditions and Surface Velocity**
 396 **Models**

397 The operating conditions of the TPS are specified by the boundary conditions, i.e., the heat
 398 flux, and the surface velocity model (SVM). Specifically, the heat flux on the Neumann
 399 BC is parametrized using $\boldsymbol{\xi}_{\text{BC}} = \{\xi_0, \xi_1, \xi_2\}$, while the SVM is parametrized using $\boldsymbol{\xi}_{\text{SVM}} =$
 400 $\{\alpha_1, \alpha_2, \alpha_3\}$. Thus, the heat flux and SVM over the i -th ablative component are expressed
 401 as,

$$q(x, t; \boldsymbol{\xi}_{\text{BC}}) = \xi_0 e^{\xi_1 x} e^{\xi_2 t}, \quad \forall x \in \Gamma_{i,q}, \quad \dot{w}_i(z_{u,i}; \boldsymbol{\xi}_{\text{SVM}}) = \alpha_i (z_{u,i} - u_{0,i}) \quad (47)$$

402 where $\Gamma_{i,q}$, $z_{u,i}$, and $u_{0,i}$ correspond to the Neumann BC surface, the PIROM's surface tem-
 403 perature prediction, and the initial temperature of the i -th ablative component, respectively.
 404 The ξ_0 controls the magnitude of the heat flux, while ξ_1 and ξ_2 control the spatial and
 405 temporal variations, respectively. The constant α_i is a small material-dependent constant
 406 determined from the B' table, specifying the ablation velocity for a given change in surface
 407 temperature.

408 **4.3 Data Generation**

409 Full-order solutions of the TPS are computed using the FEM multi-mechanics module of
 410 the **Aria** package [4], where the mesh is shown in Fig. x. The mesh consists of 2196
 411 total elements, with 366 elements for each ablative component and 1098 elements for the
 412 substrate component. All solutions are computed for one minute from an uniform initial
 413 temperature of $T(x, t_0) = 300$ K. Given an operating condition $\boldsymbol{\xi} = [\boldsymbol{\xi}_{\text{BC}}, \boldsymbol{\xi}_{\text{SVM}}]^\top$, a full-
 414 order solution consists of then collection of time-varying temperature and displacement fields
 415 $\left\{ \left(t_k, \mathbf{u}_{\text{HF}}^{(l)}(t_k), \mathbf{w}_{\text{HF}}^{(l)}(t_k), \boldsymbol{\xi}^{(l)} \right) \right\}_{k=0}^{p-1}$, where p is the number of time steps with a step size of
 416 $\Delta t \approx 10^{-3}$. The observable trajectories are representative of near-wall thermocouple sensing
 417 of hypersonic flows involving heat transfer. At each time instance t_k , a temperature reading is
 418 recorded from each ablative component using the thermocouples shown in Fig. x, resulting

419 in three temperature signals, i.e., the observables $\mathbf{z}_{textHF} \in \mathbb{R}^3$. Therefore, each full-order
 420 solution produces one trajectory of observables $\left\{ \left(t_k, \mathbf{z}_{HF}^{(l)}(t_k), \boldsymbol{\xi}^{(l)} \right) \right\}_{k=0}^{p-1}$. The goal of the
 421 PIROM is to predict the surface temperature and displacement as accurately as possible.

422 4.3.1 Definition of Training and Testing Datasets

423 The range of parameters used to generate the training and testing datasets are listed in
 424 Table [x](#). The training and testing datasets are designed, respectively, to: (1) minimize
 425 the information that the PIROM can “see”, and (2) to maximize the variability of test
 426 operating conditions to examine the PIROM’s generalization performance. A total of 110
 427 normally-distributed data points for the BC parametrization are visualized in Fig. [x](#), and
 428 the corresponding observable trajectories are shown in Fig. [x](#). The training dataset \mathcal{D}_1
 429 includes 10 trajectories with randomly selected BC parameters from the 110 points, with
 430 nominal SVM parameters $\boldsymbol{\xi}_{SVM} = \{1, 1, 1\} \times 10^{-6}$.

431 Two additional datasets are generated for testing. The dataset \mathcal{D}_2 includes the remaining
 432 100 BC parameter values not considered in \mathcal{D}_1 , and the high-fidelity simulation are generated
 433 with the same nominal SVM parameters. The dataset \mathcal{D}_3 includes 10 SVM parameter
 434 perturbations

435 The testing dataset \mathcal{D}_2 includes the remaining 100 parameter values, and the high-fidelity
 436 simulations are generated with varying SVM parameters $\boldsymbol{\xi}_{SVM}$ sampled from a uniform dis-
 437 tribution within the ranges listed in Table [x](#).

⁴³⁸ **4.4 Performance Metrics**

⁴³⁹ **4.5 Convergence Study**

⁴⁴⁰ **4.6 Generalization to Boundary Conditions**

⁴⁴¹ **4.7 Generalization to Surface Velocity Models**

⁴⁴² **4.8 Summary of Results**

⁴⁴³ **5 Conclusions**

444 A Technical Details

445 This appendix presents the technical details of the PIROM framework applied to the TPS
446 ablation problem. The first section provides the mathematical details for the definition of
447 the DG-FEM. The second section follows the projection procedures from Ref. [\[x\]](#), and demon-
448 strates the effects of coarse-graining on the advection matrix. The third section presents the
449 derivation of the LCM model from an energy-conservation perspective.

450 A.1 Full-Order Model

451 To obtain the full-order numerical solution, the governing equation is spatially discretized
452 using variational principles of Discontinuous Galerkin (DG) to result in a high-dimensional
453 system of ordinary differential equations (ODEs). The DG-FEM model is written in an
454 element-wise form, which is beneficial for subsequent derivations of the lower-order models.
455 Note that the choice of DG approach here is mainly for theoretical convenience in the sub-
456 sequent coarse-graining formulation. In the numerical results, the full-order TPS ablation
457 simulations is computed using standard FEM instead, and the equivalence between DG and
458 standard FEM is noted upon their convergence.

459 A.1.1 Domain Discretization

460 Consider a conforming mesh partition of the domain, as shown in Fig. [DOMAIN](#), where each
461 element belongs to one and only one component. Denote the collection of all M elements
462 as $\{E_i\}_{i=1}^M$. To ease the description of the DG model, a graph structure is employed. The
463 elements are treated as vertices, the set of which is denoted $\mathcal{V} = \{m\}_{m=1}^M$. Two neighboring
464 elements, E_i and E_j , are connected by an edge (i, j) , and the shared boundary between them
465 is denoted e_{ij} . The collection of all edges are denoted \mathcal{E} , and \mathcal{G} is referred to as a graph.
466 In the graph, the edges are unidirected, meaning if $(i, j) \in \mathcal{E}$ then $(j, i) \in \mathcal{E}$. Furthermore,
467 denote the neighbors of the i -th element as $\mathcal{N}_i = \{j | (i, j) \in \mathcal{E}\}$. Lastly, for the ease of

⁴⁶⁸ notation, introduce two special indices: T for the boundary of an element that overlaps with
⁴⁶⁹ the Dirichlet boundary condition, and similarly q for the Neumann boundary condition.

⁴⁷⁰ A.1.2 Weak Form of Discontinuous Galerkin Method

⁴⁷¹ Choosing appropriate basis functions ϕ_k and ϕ_l and using the Interior Penalty Galerkin
⁴⁷² (IPG) scheme [5], the variational bilinear form for eq. (1a) is,

$$\sum_{i=1}^M a_{\epsilon,i}(\phi_k, \phi_l) = \sum_{i=1}^M L_i(\phi_k) \quad (48)$$

⁴⁷³ where ϵ is an user-specified parameter and,

$$a_{\epsilon,i}(\phi_k, \phi_l) = \int_{E^{(i)}} \left(\rho c_p \phi_k \frac{\partial \phi_l}{\partial t} + \nabla \phi_k \cdot (\mathbf{k} \nabla \phi_l) - \rho c_p \phi_k \mathbf{v} \cdot \nabla \phi_l \right) dE^{(i)} \quad (49a)$$

$$= - \sum_{j \in \mathcal{N}_i \cup \{T_b\}} \int_{e_{ij}} \{ \mathbf{k} \nabla \phi_k \cdot n \} [\phi_l] de_{ij} + \epsilon \sum_{j \in \mathcal{N}_i \cup \{T_b\}} \int_{e_{ij}} \{ \mathbf{k} \nabla \phi_l \cdot n \} [\phi_k] de_{ij} \\ + \sigma \sum_{j \in \mathcal{N}_i \cup \{T_b\}} \int_{e_{ij}} [\phi_k] [\phi_l] de_{ij} \quad (49b)$$

$$L_i(v) = \epsilon \sum_{j \in \mathcal{N}_i \cup \{T_b\}} \int_{e_{ij}} (\mathbf{k} \nabla \phi_l \cdot n) T_b de_{ij} + \int_{e_{iq}} \phi_k q_b de_{iq} + \sigma \int_{e_{iT}} \phi_k T_b de_{iT} \quad (49c)$$

⁴⁷⁴ In the bi-linear form above, the notations $[]$ and $\{ \}$ are respectively the jumps and averages
⁴⁷⁵ at the boundary e_{ij} share by two elements E_i and E_j ,

$$[u] = u|_{E_i} - u|_{E_j}, \quad \{u\} = \frac{1}{2} \left(u|_{E_i} + u|_{E_j} \right), \quad \text{for } x \in e_{ij} = E_i \cap E_j$$

⁴⁷⁶ Furthermore, in the bi-linear form, the terms associated with σ are introduced to enforce
⁴⁷⁷ the Dirichlet boundary conditions; σ is a penalty factor whose value can depend on the size
⁴⁷⁸ of an element. Depending on the choice of ϵ , the bi-linear form corresponds to symmetric
⁴⁷⁹ IPG ($\epsilon = -1$), non-symmetric IPG ($\epsilon = 1$), and incomplete IPG ($\epsilon = 0$). All these schemes
⁴⁸⁰ are consistent with the original PDE and have similar convergence rate with respect to mesh

481 size. In the following derivations, the case $\epsilon = 0$ is chosen for the sake of simplicity.

482 A.1.3 Discontinuous Galerkin Model

483 Next, the DG-based model is written in an element-wise form. For the i -th element, use a
484 set of P trial functions to represent the temperature as in eq. (6). Without loss of generality,
485 the trial functions are assumed to be orthogonal, so that $\int_{E^{(i)}} \phi_k^{(i)}(x) \phi_l^{(i)}(x) dx = |E^{(i)}| \delta_{kl}$,
486 where $|E^{(i)}|$ is the area ($n_d = 2$) or volume ($n_d = 3$) of the i -th element, and δ_{kl} is the
487 Kronecker delta.

488 Using test functions same as trial functions, the dynamics $\mathbf{u}^{(i)}$ is obtained by evaluating
489 the element-wise bi-linear forms,

$$a_{\epsilon,i}(\phi_k^{(i)}, T^{(i)}) = L_i(\phi_k^{(i)}), \quad k = 1, 2, \dots, P \quad (50)$$

490 The above procedure yields,

$$\mathbf{A}^{(i)} \dot{\mathbf{u}}^{(i)} = (\mathbf{B}^{(i)} + \mathbf{C}^{(i)}(t)) \mathbf{u}^{(i)} + \sum_{j \in \mathcal{N}_i \cup \{T_b\}} \left(\mathbf{B}_{ij}^{(i)} \mathbf{u}^{(i)} + \mathbf{B}_{ij}^{(j)} \mathbf{u}^{(j)} \right) + \mathbf{f}^{(i)}(t) \quad (51)$$

491 where for $k, l = 1, 2, \dots, P$,

$$[\mathbf{A}^{(i)}]_{kl} = \int_{E^{(i)}} \rho c_p \phi_k^{(i)} \phi_l^{(i)} dE^{(i)} \quad (52a)$$

$$[\mathbf{B}^{(i)}]_{kl} = - \int_{E^{(i)}} (\nabla \phi_k^{(i)}) \cdot (\mathbf{k} \nabla \phi_l^{(i)}) dE^{(i)} \quad (52b)$$

$$[\mathbf{C}^{(i)}]_{kl} = \int_{E^{(i)}} \rho c_p \phi_k^{(i)} \mathbf{v}^{(i)} \cdot \nabla \phi_l^{(i)} dE^{(i)} \quad (52c)$$

$$[\mathbf{B}_{ij}^{(i)}] = \int_{e_{ij}} \left\{ \mathbf{k} \nabla \phi_k^{(i)} \cdot \hat{n} \right\} \phi_l^{(i)} - \sigma [\phi_k^{(i)}] \phi_l^{(i)} de_{ij} \quad (52d)$$

$$[\mathbf{B}_{ij}^{(j)}] = \int_{e_{ij}} - \left\{ \mathbf{k} \nabla \phi_k^{(i)} \cdot \hat{n} \right\} \phi_l^{(j)} + \sigma [\phi_k^{(i)}] \phi_l^{(j)} de_{ij} \quad (52e)$$

$$[\mathbf{f}^{(i)}]_k = \int_{e_{iq}} \phi_k^{(i)} q_b de_{iq} + \sigma \int_{e_{iT}} \phi_k^{(i)} de_{iT} \quad (52f)$$

492 The matrices $\mathbf{A}^{(i)} \in \mathbb{R}^{P \times P}$, $\mathbf{B}^{(i)} \in \mathbb{R}^{P \times P}$, and $\mathbf{C}^{(i)} \in \mathbb{R}^{P \times P}$ are respectively the capacitance,
 493 conductivity, and advection matrices for element i . These matrices depend on ρ , c_p , \mathbf{k} , and
 494 \mathbf{v} , and hence can be non-linear functions of $\mathbf{u}^{(i)}$. Since the trial functions are orthogonal, if
 495 ρc_p is constant within an element, $\mathbf{A}^{(i)}$ is diagonal; otherwise, \mathbf{A}_i is symmetric and positive
 496 definite as $\rho c_p > 0$.

497 For compactness, the element-wise model in eq. (51) is also written in matrix form,

$$\mathbf{A}(\dot{\mathbf{u}}) = [\mathbf{B}(\mathbf{u}) + \mathbf{C}(\mathbf{u})] \mathbf{u} + \mathbf{f}(t) \quad (53)$$

498 where $\mathbf{u} = [\mathbf{u}^{(1)}, \mathbf{u}^{(2)}, \dots, \mathbf{u}^{(M)}]^T \in \mathbb{R}^{MP}$ includes all DG variables, $\mathbf{f} = [\mathbf{f}^{(1)}, \mathbf{f}^{(2)}, \dots, \mathbf{f}^{(M)}]^T \in$
 499 \mathbb{R}^{MP} , \mathbf{A} and \mathbf{C} are matrices of M diagonal blocks whose i -th blocks are $\mathbf{A}^{(i)}$ and $\mathbf{C}^{(i)}$, and
 500 \mathbf{B} is a matrix of $M \times M$ blocks whose (i, j) -th block is,

$$\mathbf{B}_{ij} = \begin{cases} \mathbf{B}^{(i)} + \sum_{j \in \mathcal{N}_i \cup \{T_b\}} \mathbf{B}_{ij}^{(i)}, & i = j \\ \mathbf{B}_{ij}^{(j)}, & i \neq j \end{cases} \quad (54)$$

501 The dependency of \mathbf{A} , \mathbf{B} , and \mathbf{C} on \mathbf{u} is explicitly noted in eq. (53), which is the source of
 502 non-linearity in the current TPS problem. Moreover, the mesh velocity \mathbf{v} varies with space
 503 and time, and thus the advection matrix \mathbf{C} varies with time as a function of q_b .

504 A.2 Coarse-Graining of Dynamics

505 The LCM is obtained by coarse-graining the full-order DG-FEM. This coarse-graining proce-
 506 dure produces resolved $\mathbf{r}^{(1)}(\mathbf{u}, t)$ and residual $\mathbf{r}^{(2)}(\mathbf{u}, t)$ dynamics as in eq. (23). This section
 507 presents the detail derivations and magnitude analysis for the resolved and residual dynam-
 508 ics.

509 **A.2.1 Resolved Dynamics**

510 Using eq. (20), the resolved dynamics is computed as follows,

$$\mathbf{r}^{(1)}(\mathbf{u}, t) = \mathcal{P} [\Phi^+ \mathbf{A}(\mathbf{u})^{-1} (\mathbf{B}(\mathbf{u})\mathbf{u} + \mathbf{C}(\mathbf{u})\mathbf{u} + \mathbf{f}(t))] \quad (55a)$$

$$\begin{aligned} &= \Phi^+ \mathbf{A}(\mathbf{P}\mathbf{u})^{-1} \mathbf{P}\mathbf{B}(\mathbf{P}\mathbf{u}) \mathbf{P}\mathbf{u} + \Phi^+ \mathbf{A}(\mathbf{P}\mathbf{u})^{-1} \mathbf{P}\mathbf{C}(\mathbf{P}\mathbf{u}) \mathbf{P}\mathbf{u} \\ &\quad + \Phi^+ \mathbf{A}(\mathbf{P}\mathbf{u})^{-1} \mathbf{P}\mathbf{f}(t, \mathbf{P}\mathbf{u}) \end{aligned} \quad (55b)$$

$$\begin{aligned} &= \underbrace{\Phi^+ \mathbf{A}(\Phi\bar{\mathbf{u}})^{-1} \Phi}_{\#1} \underbrace{\Phi^+ \mathbf{B}(\Phi\bar{\mathbf{u}}) \Phi\bar{\mathbf{u}}}_{\#2} + \Phi^+ \mathbf{A}(\Phi\bar{\mathbf{u}})^{-1} \Phi \underbrace{\Phi^+ \mathbf{C}(\Phi\bar{\mathbf{u}}) \Phi\bar{\mathbf{u}}}_{\#3} \\ &\quad + \Phi^+ \mathbf{A}(\Phi\bar{\mathbf{u}})^{-1} \Phi \underbrace{\Phi^+ \mathbf{f}(t, \Phi\bar{\mathbf{u}})}_{\#4} \end{aligned} \quad (55c)$$

511 Detailed derivations for the #1, #2, and #4 terms can be found in Ref. [x]. The effects of
512 coarse-graining on the advection term #3 are analyzed next.

513 **Term #3** The $\mathbf{C}(\mathbf{u}) \in \mathbb{R}^{MP \times MP}$ matrix contains M diagonal of size $P \times P$, since the
514 basis functions are defined locally on each element. Therefore, $[\mathbf{C}(\mathbf{u})]_{ij} = \mathbf{0}$ for all $i \neq j$ with
515 $i, j = 1, 2, \dots, M$. It follows that for $k, l = 1, 2, \dots, N$,

$$[\Phi^+ \mathbf{C}(t, \Phi\bar{\mathbf{u}}) \Phi]_{kl} = \sum_{i=1}^M \sum_{j=1}^M \boldsymbol{\varphi}_i^{k+} [\mathbf{C}(t, \Phi\bar{\mathbf{u}})]_{ij} \boldsymbol{\varphi}_j^l \quad (56a)$$

$$= \sum_{i=1}^M \boldsymbol{\varphi}_i^{k+} [\mathbf{C}(t, \Phi\bar{\mathbf{u}})]_{ii} \boldsymbol{\varphi}_i^l \quad (56b)$$

$$= \sum_{i \in \mathcal{V}_k} \boldsymbol{\varphi}_i^{k+} [\mathbf{C}(t, \Phi\bar{\mathbf{u}})]_{ii} \boldsymbol{\varphi}_i^l \quad (56c)$$

516 where in the second row, the fact that $[\mathbf{C}(\mathbf{u})]_{ij} = 0$ for all $i \neq j$ is used, and in the last row,
517 the fact that $\boldsymbol{\varphi}_i^{k+} = 0$ for all $i \notin \mathcal{V}_k$ is used. Now, considering that $[\mathbf{C}(\mathbf{u})]_{ii}$ has a (1, 1)-th
518 zero element, i.e., $[\mathbf{C}(t, \Phi\bar{\mathbf{u}})]_{ii} = 0$, and that if $k \neq l$ then $i \notin \mathcal{V}_l$ and thus $\boldsymbol{\varphi}_i^l = \mathbf{0}$, it follows

519 that for some index $i \in \mathcal{V}_k$,

$$\boldsymbol{\varphi}_i^{k+} [\mathbf{C}(t, \Phi \bar{\mathbf{u}})]_{ii} \boldsymbol{\varphi}_i^l = \boldsymbol{\varphi}_i^{k+} [\mathbf{C}(t, \Phi \bar{\mathbf{u}})]_{ii} \boldsymbol{\varphi}_i^k = \frac{|E_i|}{|\Omega_k|} [C_{11}(t, \Phi \bar{\mathbf{u}})]_{ii} = 0 \quad (57)$$

520 The matrix $[\Phi^+ \mathbf{C}(t, \Phi \bar{\mathbf{u}}) \Phi]_{kl} = 0$ for all $k, l = 1, 2, \dots, N$, and thus,

$$\bar{\mathbf{C}}(t, \bar{\mathbf{u}}) = \Phi^+ \mathbf{C}(t, \Phi \bar{\mathbf{u}}) \Phi = \mathbf{0} \quad (58)$$

521 as indicated by the LCM in eq. (9).

522 A.2.2 Magnitude Analysis for Residual Dynamics

523 Next, the magnitude of the residual dynamics $\mathbf{r}^{(2)}(\mathbf{u}, t)$ is analyzed to pinpoint the missing
524 physics in the LCM. By definition,

$$\mathbf{r}^{(2)}(\mathbf{u}, t) = \dot{\bar{\mathbf{u}}} - \mathbf{r}^{(1)}(\bar{\mathbf{u}}, t) \quad (59a)$$

$$= \Phi^+ \mathbf{r}(\mathbf{u}, t) - \mathbf{r}^{(1)}(\mathbf{u}, t) \quad (59b)$$

$$\begin{aligned} &= \underbrace{\Phi^+ \mathbf{A}(\mathbf{u})^{-1} \mathbf{B}(\mathbf{u}) \mathbf{u} - \bar{\mathbf{A}}(\bar{\mathbf{u}})^{-1} \bar{\mathbf{B}}(\bar{\mathbf{u}}) \bar{\mathbf{u}}}_{\#1} + \underbrace{\Phi^+ \mathbf{A}(\mathbf{u})^{-1} \mathbf{C}(\mathbf{u}) \mathbf{u} - \bar{\mathbf{A}}(\bar{\mathbf{u}})^{-1} \bar{\mathbf{C}}(t, \bar{\mathbf{u}}) \bar{\mathbf{u}}}_{\#2} \\ &\quad + \underbrace{\Phi^+ \mathbf{A}(\mathbf{u})^{-1} \mathbf{f}(t) - \bar{\mathbf{A}}(\bar{\mathbf{u}})^{-1} \bar{\mathbf{f}}(t)}_{\#3} \end{aligned} \quad (59c)$$

525 The magnitude analysis for terms $\#1$ and $\#3$ can be found in Ref. [\[x\]](#). The analysis for term
526 $\#2$ is presented next. Let $\mathbf{D}(\bar{\mathbf{u}}) = \mathbf{A}(\Phi \bar{\mathbf{u}})^{-1} \mathbf{P} \mathbf{C}(t, \Phi \bar{\mathbf{u}})$, then,

$$\Phi^+ \mathbf{A}(\mathbf{u})^{-1} \mathbf{C}(\mathbf{u}) \mathbf{u} - \bar{\mathbf{A}}(\bar{\mathbf{u}})^{-1} \bar{\mathbf{C}}(t, \bar{\mathbf{u}}) \bar{\mathbf{u}} \quad (60a)$$

$$= \Phi^+ \mathbf{A}(\mathbf{u})^{-1} \mathbf{C}(\mathbf{u}) \mathbf{u} - \Phi^+ \mathbf{A}(\Phi \bar{\mathbf{u}})^{-1} \mathbf{P} \mathbf{C}(t, \Phi \bar{\mathbf{u}}) \Phi \Phi^+ \mathbf{u} \quad (60b)$$

$$= \Phi^+ \mathbf{A}^{-1}(\mathbf{u}) \mathbf{C}(\mathbf{u}) \mathbf{u} - \Phi^+ \mathbf{D}(\bar{\mathbf{u}}) \Phi \Phi^+ \mathbf{u} \quad (60c)$$

$$(60d)$$

527 where $\mathbf{P} = \Phi\Phi^+$. Thus,

$$\|\Phi^+ \mathbf{A}(\mathbf{u})^{-1} \mathbf{C}(\mathbf{u}) \mathbf{u} - \bar{\mathbf{A}}^{-1}(\bar{\mathbf{u}}) \bar{\mathbf{C}}(t, \bar{\mathbf{u}}) \bar{\mathbf{u}}\| \quad (61a)$$

$$\leq \|\Phi^+ \mathbf{A}^{-1}(\mathbf{u}) \mathbf{C}(\mathbf{u}) \mathbf{u} - \Phi^+ \mathbf{D}(\bar{\mathbf{u}}) \mathbf{u}\| + \|\Phi^+ \mathbf{D}(\bar{\mathbf{u}}) \mathbf{u} - \Phi^+ \mathbf{D}(\bar{\mathbf{u}}) \Phi \Phi^+ \mathbf{u}\| \quad (61b)$$

$$\leq \|\Phi^+\| \underbrace{\|\mathbf{A}^{-1}(\mathbf{u}) \mathbf{C}(\mathbf{u}) \mathbf{u} - \mathbf{D}(\bar{\mathbf{u}}) \mathbf{u}\|}_{\#1} + \|\Phi^+ \mathbf{D}(\bar{\mathbf{u}})\| \underbrace{\|\mathbf{u} - \Phi \Phi^+ \mathbf{u}\|}_{\#2} \quad (61c)$$

528 where term $\#2$ is due to the appriximation of non-uniform temperaeture as constants, and

529 term $\#1$ is the error in the advection dynamics due to coarse-graining.

530 A.3 Lumped Capacitance Model

531 The following assumptions are employed: (1) the temperature in component (i) is described
 532 by a scalar time-varying average temperature $\bar{u}^{(i)}$, (2) between neighboring components (i)
 533 and (j) the heat flux is approximated as,

$$q_{ij} = \frac{\bar{u}^{(j)} - \bar{u}^{(i)}}{R_{ij}} \quad (62)$$

534 where R_{ij} is the thermal resistance. Empirically, for a component of isotropic heat conduc-
 535 tivity k , length ℓ , and cross-section area A , the thermal resistance is $R = \ell/kA$. Between
 536 components i and j , define $R_{ij} = R_i + R_j$. In addition, the heat flux due to Dirichlet
 537 boundary condition is computed as $q_{iT} = (T_b - \bar{u}^{(i)})/R_i$.

538

At component i , the dynamics of LCM are given by,

$$\int_{E^{(i)}} \rho c_p \dot{\bar{u}}^{(i)} dE^{(i)} = \left(\sum_{j \in \mathcal{N}_i} \int_{e_{ij}} \frac{\bar{u}^{(j)} - \bar{u}^{(i)}}{R_{ij}} de_{ij} \right) + \int_{e_{iq}} q_b de_{iq} + \int_{e_{iT}} \frac{T_b - \bar{u}^{(i)}}{R_i} de_{iT} \quad (63a)$$

$$\bar{A}^{(i)} \dot{\bar{u}}^{(i)} = \left(\sum_{j \in \mathcal{N}_i} \frac{|e_{ij}|}{R_{ij}} (\bar{u}^{(j)} - \bar{u}^{(i)}) \right) + |e_{iq}| \bar{q}^{(i)} + \frac{|e_{iT}|}{R_i} (\bar{T}^{(i)} - \bar{u}^{(i)}) \quad (63b)$$

$$= \sum_{j \in \mathcal{N}_i} \left(-\frac{|e_{ij}|}{R_{ij}} \bar{u}^{(i)} + \frac{|e_{ij}|}{R_{ij}} \bar{u}^{(j)} \right) + \left(-\frac{|e_{iT}|}{R_i} \bar{u}^{(i)} \right) + \left(|e_{iq}| \bar{q}^{(i)} + \frac{|e_{iT}|}{R_i} \bar{T}^{(i)} \right) \quad (63c)$$

$$= \sum_{j \in \mathcal{N}_i \cup \{T_b\}} \left(\bar{B}_{ij}^{(i)} \bar{u}^{(i)} + \bar{B}_{ij}^{(j)} \bar{u}^{(j)} \right) + \bar{f}^{(i)} \quad (63d)$$

539 where in eq. (63b) $|e|$ denotes the length ($d = 2$) or area ($d = 3$) of a component boundary
 540 e . The $\bar{A}^{(i)}$, $\bar{B}_{ij}^{(i)}$, and $\bar{B}_{ij}^{(j)}$ quantities are provided in eq. (12).

541 The lumped-mass representation for the four-component TPS is shown in Fig. 2. Let v_i
 542 represent the area of the i -th element, $\bar{\rho c}_{p,i}$, the heat capacity evaluated using the average
 543 temperature $\bar{u}^{(i)}$, and $1/R_{ij} = 1/R_i(\bar{u}^{(i)}) + 1/R_j(\bar{u}^{(j)})$ the equivalent thermal resistance
 544 between elements i and j . Leveraging the formulas from eqs. (11b) and (12), the LCM
 545 matrices are given by,

$$\bar{\mathbf{A}} = \begin{bmatrix} \bar{\rho c}_{p,1} v_1 & 0 & 0 & 0 \\ 0 & \bar{\rho c}_{p,2} v_2 & 0 & 0 \\ 0 & 0 & \bar{\rho c}_{p,3} v_3 & 0 \\ 0 & 0 & 0 & \bar{\rho c}_{p,4} v_4 \end{bmatrix}, \quad (64a)$$

$$\bar{\mathbf{B}} = \begin{bmatrix} \frac{1}{R_{12}} + \frac{1}{R_{14}} & -\frac{1}{R_{12}} & 0 & -\frac{1}{R_{14}} \\ -\frac{1}{R_{12}} & \frac{1}{R_{12}} + \frac{1}{R_{24}} + \frac{1}{R_{23}} & -\frac{1}{R_{23}} & -\frac{1}{R_{24}} \\ 0 & -\frac{1}{R_{32}} & \frac{1}{R_{32}} + \frac{1}{R_{34}} & -\frac{1}{R_{34}} \\ -\frac{1}{R_{14}} & -\frac{1}{R_{24}} & -\frac{1}{R_{34}} & \frac{1}{R_{14}} + \frac{1}{R_{24}} + \frac{1}{R_{34}} \end{bmatrix}, \quad \bar{\mathbf{f}} = \begin{bmatrix} \bar{q}^{(1)} \\ \bar{q}^{(2)} \\ \bar{q}^{(3)} \\ 0 \end{bmatrix} \quad (64b)$$

546 **References**

- 547 [1] Adam J. Amar, A. Brandon Oliver, Benjamin S. Kirk, Giovanni Salazar, and Justin
548 Droba. Overview of the charring ablator response (char) code. In AIAA, editor, *AIAA*
549 *Aviation Forum*, 2016.
- 550 [2] Guy L. Bergel, Frank B. Beckwith, Gabel J. de Frias, Kevin M. Manktelow, Mark T.
551 Merewether, Scott T. Miller, Krishen J. Parmar, Timothy S. Shelton, Jesse T. Thomas,
552 Jeremy T. Trageser, Benjamin T. Treweek, Michael V. Veilleux, and Ellen B. Wagman.
553 *Sierra/SolidMechanics 5.6 User's Manual*, 2022.
- 554 [3] Ricky T. Q. Chen, Yulia Rubanova, Jesse Bettencourt, and David Duvenaud. Neural
555 ordinary differential equations, 2019.
- 556 [4] Jonathan Clausen, Victor Brunini, Lincoln Collins, Robert C Knaus, Alec Kucala,
557 Stephen Lin, Daniel Robert Moser, Malachi Phillips, Thomas Michael Ransegnola,
558 Samuel Ramirez Subia, et al. Sierra multimechanics module: Aria verification manual-
559 version 5.22. Technical report, Sandia National Lab.(SNL-NM), Albuquerque, NM
560 (United States), 2024.
- 561 [5] Gary Cohen and Sebastien Pernet. *Finite Element and Discontinuous Galerkin Methods*
562 *for Transient Wave Equations*. Springer Dordrecht, Le Chesnay and Toulouse France,
563 2018.
- 564 [6] Matthew Gasch, Keith Peterson, Mairead Stackpoole, Ethiraj Venkatapathy, Gregory
565 Gonzales, and Kyle Hendrickson. Development of advanced ablative carbon phenolic
566 tps for future nasa missions and commercial space. In *38th Annual Small Satellite*
567 *Conference*, Logan, Utah, May 2024.
- 568 [7] Frank P. Incropera, David P. DeWitt, Theodore L. Bergman, and Adrienne S. Lavine.
569 *Fundamentals of Heat and Mass Transfer*. Wiley, Hoboken, NJ, 7th edition, 2011.

- 570 [8] R. J. Klock and Carlos Cesnik. Nonlinear thermal reduced-order modeling for hypersonic
571 vehicles. *AIAA Journal*, 55(7), 2017.
- 572 [9] Eric Parish and Karthik Duraisamy. Non-markovian closure models for large eddy
573 simulations using the mori-zwanzig formalism. *Phys. Rev. Fluids*, 2:014604, Jan 2017.
- 574 [10] Eric Parish and Karthik Duraisamy. A unified framework for multiscale modeling using
575 the mori-zwanzig formalism and the variational multiscale method. *ArXiv*, 12 2017.
- 576 [11] Eric Parish and Karthik Duraisamy. *Coarse-Graining Turbulence Using the
577 Mori-Zwanzig Formalism*. Cambridge University Press, Cambridge, 2025.
- 578 [12] Carlos A. Vargas Venegas, Daning Huang, Patrick Blonigan, and John Tencer. Physics-
579 infused reduced-order modeling for analysis of multi-layered hypersonic thermal protec-
580 tion systems. *ArXiv*, 2025.
- 581 [13] Yin Yu, John Harlim, Daning Huang, and Yan Li. Learning coarse-grained dynamics
582 on graph. *arXiv preprint arXiv:2405.09324*, 2024.